



Al-Rawhani, M. A. et al. (2019) Multimodal integrated sensor platform for rapid biomarker detection. *IEEE Transactions on Biomedical Engineering*, (doi: [10.1109/TBME.2019.2919192](https://doi.org/10.1109/TBME.2019.2919192)).

This is the author's final accepted version.

There may be differences between this version and the published version. You are advised to consult the publisher's version if you wish to cite from it.

<http://eprints.gla.ac.uk/187249/>

Deposited on: 29 May 2019

Enlighten – Research publications by members of the University of Glasgow
<http://eprints.gla.ac.uk>

Multimodal Integrated Sensor Platform for Rapid Biomarker Detection

Mohammed A. Al-Rawhani, Chunxiao Hu, Christos Giagkoulovits, *Member, IEEE*, Valerio F. Annese, Boon Chong Cheah, James Beeley, Srinivas Velugotla, Claudio Accarino, James P. Grant, Srinjoy Mitra, *Member, IEEE*, Michael P. Barrett, Sandy Cochran, *Member, IEEE*, and David R. S. Cumming, *Fellow, IEEE*

Abstract—Precision metabolomics and quantification for cost-effective, rapid diagnosis of disease are key goals in personalized medicine and point-of-care testing. Presently, patients are subjected to multiple test procedures requiring large laboratory equipment. Microelectronics has already made modern computing and communications possible by integration of complex functions within a single chip. As More than Moore technology increases in importance, integrated circuits for densely patterned sensor chips have grown in significance. Here, we present a versatile single CMOS chip forming a platform to address personalized needs through on-chip multimodal optical and electrochemical detection that will reduce the number of tests that patients must take. The chip integrates interleaved sensing subsystems for quadruple-mode colorimetric, chemiluminescent, surface plasmon resonance and hydrogen ion measurements. These subsystems include a photodiode array and a single photon avalanche diode array, with some elements functionalized to introduce a surface plasmon resonance mode. The chip also includes an array of ion sensitive field effect transistors. The sensor arrays are distributed uniformly over an active area on the chip surface in a scalable and modular design. Bio-functionalization of the physical sensors yields a highly selective simultaneous multiple-assay platform in a disposable format. We demonstrate its versatile capabilities through quantified bioassays performed on-chip for glucose, cholesterol, urea and urate, each within their naturally occurring physiological range.

Index Terms— CMOS, multimodality, diagnosis, biomarker, detection, colorimetric, chemiluminescence, pH measurements, surface plasmon resonance, nanodiscs, plasmon filters, SPAD, Photodiode. ISFET.

I. INTRODUCTION

Optical and electrochemical sensing techniques are widely used in biomedical science and clinical medicine. Colorimetric analysis [1], chemiluminescence [2], fluorescence [3], surface plasmon resonance (SPR) [4], potentiometry and

amperometry [5] are commonly employed optical and electrochemical modalities for biosensing and quantification. Both have been employed in clinical diagnostics, DNA sequencing [2], [6], immunoassays [5], [7], metabolite quantification [8]–[10], and protein detection [11], [12] for the identification of diseases at an early stage using biomarkers [13].

The diversity in the range of biomarkers is conventionally addressed by the use of multiple single-mode, bench-top laboratory instruments [14]. For example, detecting a specific biomarker (e.g. a metabolite) using a colorimetric assay requires a spectrophotometer comprising an illumination source and a photosensitive light detector to measure enzymatic activity by means of a colour change [15]. A chemiluminescence assay does not require an illumination source but needs an instrument with a highly sensitive light detector such as a charge-coupled device (CCD) or a photomultiplier tube (PMT) to measure weak light emission [16]. Surface plasmon resonance (SPR) provides a further optical modality to detect biological or chemical activities by measuring localized changes in refractive index at the functionalized surface of a metal such as gold when a target analyte is present [4].

In electrochemical sensing, ionic concentrations are measured either by potentiometry e.g. with a glass electrode for pH measurements, or voltammetry using a potentiostat, to induce and measure charge transfer reactions [17], [18]. These instruments use electrodes to detect metabolites; for example, blood glucose self-monitoring devices use enzymes to produce hydrogen ions in proportion to the metabolite concentration [8], [19]. Presently, all these modalities rely on discrete and specialized apparatus. However, complementary metal oxide semiconductor (CMOS) technology presents a new alternative, with integration of many of the sensor and electronic circuits

This work was supported by the Engineering and Physical Sciences Research Council grant EP/K021966/1.

M. A. Al-Rawhani was with the School of Engineering, University of Glasgow. He is now with STMicroelectronics (R&D) Ltd., Edinburgh, EH12 7BF, UK (email: mohammed.al-rawhani@glasgow.ac.uk).

C. Hu, C. Giagkoulovits, V. F. Annese, J. Beeley, S. Velugotla, C. Accarino, J. P. Grant, S. Cochran and D. R. S. Cumming are with the School of Engineering, University of Glasgow, Glasgow, G12 8LT, UK.

B. C. Cheah was with the School of Engineering, University of Glasgow. He is now with ams Netherlands BV, Eindhoven, 5656 AE, The Netherlands.

S. Mitra was with the School of Engineering, University of Glasgow. He is now with the Institute for Integrated Micro and Nano Systems (IMNS), University of Edinburgh, Edinburgh, EH9 3FF, UK.

M. P. Barrett is with the Institute of Infection, Immunity and Inflammation University of Glasgow, Glasgow, G12 8QQ, UK.

All our datasets can be accessed at <http://dx.doi.org/10.5525/gla.researchdata.825>

Copyright (c) 2017 IEEE. Personal use of this material is permitted. However, permission to use this material for any other purposes must be obtained from the IEEE by sending an email to pubs-permissions@ieee.org.

required on a single chip [20]–[24]. This opens a route to bespoke, specific diagnosis and disease management at low-cost and readily deployed outside a specialized laboratory. Integration of multiple measurement modalities on a single chip enables multiple biomarker tests from a single sample, with the potential to accelerate and improve care pathways and to increase convenience for patients.

CMOS microelectronics is the foundation of modern computing and communication technology, facilitating mass manufacture of today’s sophisticated consumer and commercial systems [25]. Research has demonstrated that CMOS technology is versatile, comprising a rich materials palette capable of exploitation in unconventional markets. Careful design and advanced fabrication techniques have allowed CMOS to address applications such as chemical sensing, gas detection and genomics [26]–[29]. Here we show that innovative design and technology integration create new opportunities to exploit CMOS technology in metabolomics and biomarker measurement. Unlike genomics that reveal an individual’s innate propensity towards disease, we focus on metabolomics, or phenotypical markers, that have proven utility in monitoring the individual’s current physiological state [14], [30]–[32].

Thousands of metabolites can be found in human serum alone, many of which can be used as biomarkers for diseases and functional evaluation [31]. However, the measurement challenge is distinct from that of genetic sequencing since the physicochemical properties of metabolites are diverse and dynamic concentration varies over many orders of magnitude in human body fluids. Highly differentiated sensors are required using optical and electrochemical modalities and metabolite specific biofunctionalization of sensors in an array.

II. DISPOSABLE MULTIMODAL CMOS PLATFORM

We have used a CMOS process, for the first time to the authors’ knowledge, to allow interleaving of four widely used laboratory measurement modalities: colorimetry, chemiluminescence, SPR and hydrogen ion (H^+) measurement. The data presented exploit devices made without deviation from standard CMOS device technology. Specific measurements for biochemical sensing are achieved after nanofabrication of optical structures and biofunctionalization in a post-foundry process step.

The chip has two optical sensor arrays based on photodiodes (PDs) and single photon avalanche diodes (SPADs). These are both implemented using the foundry technology without modification. The SPAD array is used for chemiluminescence detection since high sensitivity is required. In contrast, the colorimetric mode requires an illumination source, therefore the PD is suitable as it is not susceptible to saturation by ambient light. Enzyme-based assays coupled to dyes that change colour in the presence of the reaction products are exploited to quantify the metabolite turned over by the enzyme. The use of PDs and SPADs in combination extends the optical dynamic range, for the first-time allowing integration of colorimetric measurements for high concentration metabolites and chemiluminescence measurement for low concentration metabolites.

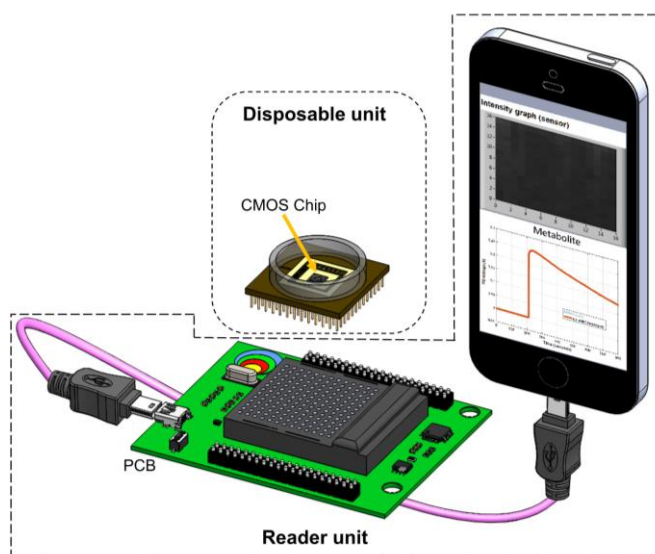


Fig. 1. Working principle of the prototype portable CMOS platform. The system comprises a disposable cartridge containing the CMOS chip and a reader connected to a tablet PC or Smart Phone.

Further physical functionalization of the sensors can be achieved by additional post-foundry nanofabrication on to either the PDs or the SPADs. Arrays of gold nanodiscs over an individual sensor fabricated in this manner exhibit SPR; when a fixed wavelength light source is applied, any change in the resonant wavelength caused by a change in the refractive index at the metal surface modifies the optical transmission of the nanodisc array and can be measured by the PDs or SPADs. In addition to the optical sensor arrays, the chip has an ion sensitive field effect transistor (ISFET) array selective for H^+ to provide an electrochemical measurement capability for metabolite detection via proton release.

The multi-sensor array chip forms a platform in which a wide-range of application-specific bioassays can be rapidly employed and used selectively with one of the integrated modalities. The use of an array for each modality offers the potential to selectively functionalize parts of the array for different assays. By so doing, we create the potential for a broad-spectrum diagnostic tool that will eliminate the need for multiple repeated procedures that cause patient discomfort and alarm. Fig. 1 illustrates the concept of the proposed portable platform with a disposable CMOS-based cartridge.

III. SCALABLE MODULAR DESIGN OF THE CMOS CHIP

The CMOS chip incorporates a 16×16 array of elements, each with three “pixels” for, respectively, a PD, a SPAD and an ISFET, giving 256 of each type of sensor in the array. This arrangement ensures an even distribution of sensors for each modality across the active area of the chip allowing a scalable modular design as illustrated in Fig. 2. In addition to the capacity to selectively functionalize parts of the array for different assays, the array can be used to exploit the statistical phenomenon of averaging signals from independent Gaussian noise sources, either over time or spatially, to improve the overall system sensitivity. The chip integrates addressing blocks to allow each sensor array to be controlled and operated independently or simultaneously as required, as shown in

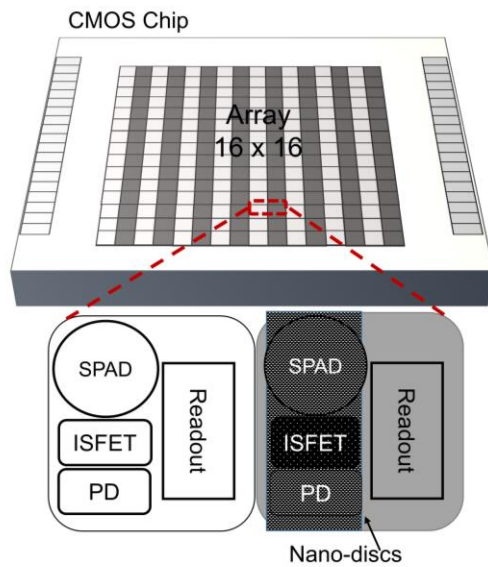


Fig. 2. Layout of the CMOS chip integrating 16 x 16 elements: each integrates a SPAD, an ISFET and a PD with their readout circuits. Columns were alternatively patterned with Au nanodiscs to build SPR sensors.

Fig. 3. Whilst full operation of all aspects of the chip simultaneously is possible, the device integrates power-down switches (Fig. 3) for the SPAD and ISFET arrays to selectively manage and reduce power consumption.

The PD pixel, Fig. 3, incorporates a P-N junction with a three-transistor (M_{1p} , M_{2p} and M_{3p}) active photosensor design [33]. The pixel's exposure is controlled by a global shutter input, V_{rst} . Depending on the integration time, a given photocurrent, I_{ph} , corresponds to a given voltage, V_d , across the PD. The values of V_d for all pixels are measured and streamed to a single output pad using independent 4-bit row and column decoders.

The SPAD pixel, incorporates a P-N junction with a high breakdown voltage operated in the Geiger mode at a reverse bias voltage, $HV - V_{Bias}$, above its breakdown voltage. The SPAD uses a transistor, M_{1s} , to quench the avalanche process triggered by a photon incident on its active area, resulting in a stream of output pulses proportional in count-rate to the number of incident photons. The pulses drive a controlled inverter, M_{2s} and M_{3s} , and are then counted by a dedicated 16-bit counter outside the aperture of the array. The SPAD array is scanned using a rolling shutter scheme in which the 16 SPADs from each column are activated sequentially using a 4-bit address decoder, reducing power consumption. The column SPADs' outputs are connected to 16 counters. A second decoder feeds their outputs sequentially into a 1-bit digital output via a serializer. All transistors in the SPAD array are isolated using a high voltage (HV) deep n-well to reduce crosstalk with other sensors.

Half of the optical sensors are modified to make SPR sensors on-chip. Most SPR systems adopt the Kretschmann configuration, using a plane-polarized light with a fixed angle of incidence, and a CCD camera to detect the wavelength of light reflected from a gold sheet [34], [35]. Highly selective biomarker detection that involves binding to immobilized

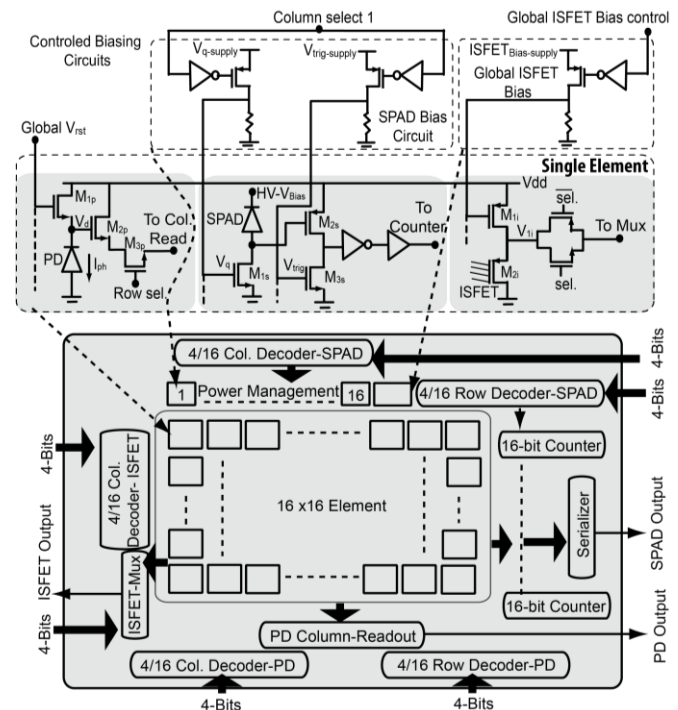


Fig. 3. Block diagram of the CMOS chip, showing the independent addressing and readout architectures of the multiple sensing techniques. The magnified section shows the schematic of the readout circuits of the three sensors: SPAD, PD and ISFET.

receptors is a common application of SPR in diagnostics, providing the perturbation to the refractive index at the gold surface that underpins the method [4]. For the on-chip SPR sensors, gold nanodisc optical filters were post-processed on to the PDs and SPADs located in alternate columns, resulting in an array of 128 filtered (even columns) and 128 unfiltered (odd columns) PDs and SPADs (Fig. 2). The post-processing fabrication steps and a detail of the fabricated structure is shown in Fig. 4 (a). The nanostructures were designed to have a fixed disc diameter and fixed pitch. These parameters, together with the refractive index of the sensor's environment, determine the resonant wavelength of the nanostructures that collectively act as an optical band-stop filter. Au was chosen to create the plasmonic structures for its biocompatible properties and because it is a noble metal. The plasma frequency in Au occurs at approximately 450 nm. SPR effects that are used for sensing are strongest at longer wavelengths. Si photodiodes exhibit excellent sensitivity above 630 nm. The nanodiscs are also easier to fabricate for longer wavelengths owing to scaling. These considerations motivated our choice of dimensions. The resonance response of the filters was optimized using finite element analysis software (Multiphysics®, COMSOL Ltd, Cambridge, UK). The discs were 60 nm thick, 200 nm in diameter and the pitch was 450 nm. Prior to fabricating the nanodisc array, a 500 nm thick layer of SiO_2 was deposited using plasma-enhanced chemical vapor deposition (PECVD), as shown in Fig. 4(a), (ii). The nanodiscs were selectively fabricated on alternate columns, with the other columns left blank. A poly(methyl methacrylate) (PMMA) bi-layer was patterned to create the nanodisc array using electron beam lithography, and developed with IPA:MIBK (3:1) (Fig. 4(a)

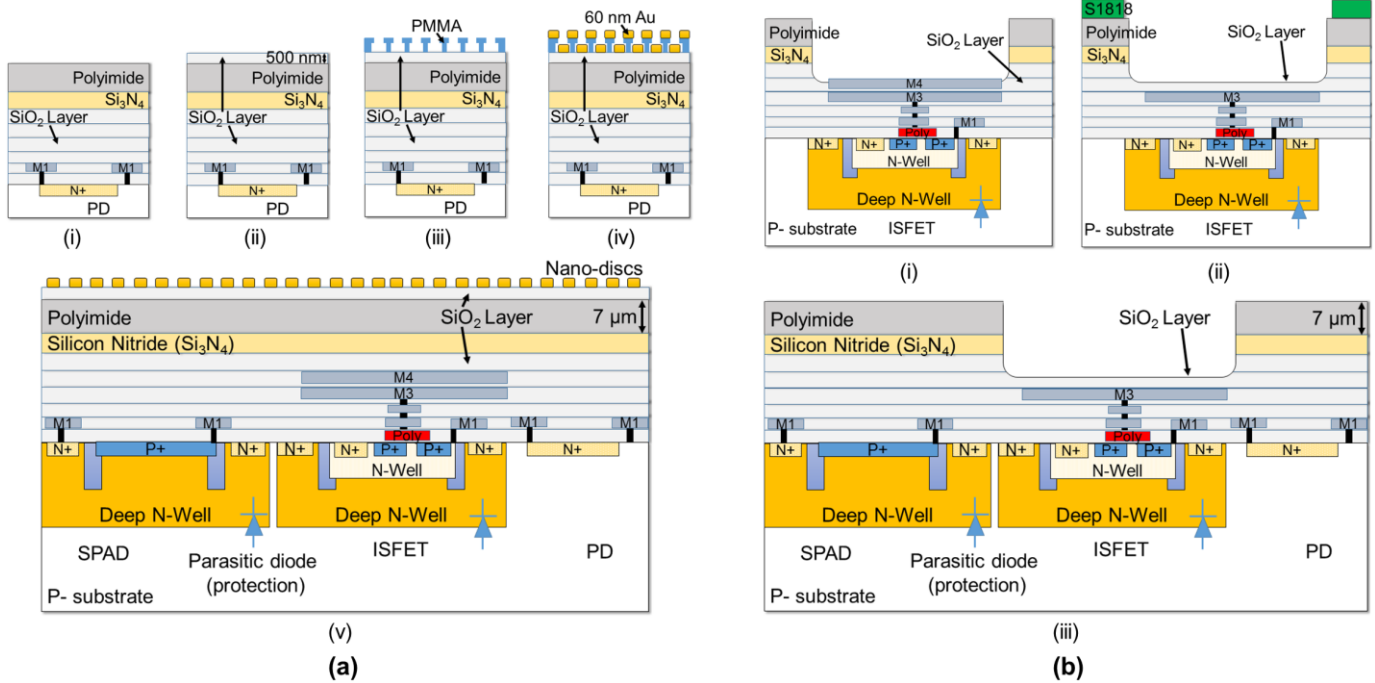


Fig. 4. A cross-section of an element showing the SPAD, PD and ISFET implementation in the CMOS process and the post-processing fabrication steps for (a) an element of an even column patterned with nanodiscs on the chip surface and (b) an element of an odd column where a thin layer of SiO₂ was selectively revealed on top of the ISFET (column without nanodisc post-processing).

(iii). 60 nm of gold was evaporated on top of 3 nm of Ti, for adhesion purposes (Fig. 4(a) (iv)). Finally, the resist and unwanted metal was removed by lift off in acetone to leave the final structure (Fig. 4(a) (v)). The resonant wavelength from simulation was 750 nm which agreed well with the experimental results from fabricated nanodiscs on a glass slide as shown in Fig. 5 (a). Further experiments were conducted as a feasibility study, using nanodiscs on glass to show a resonant wavelength shift as a function of different glycerol concentrations, as it is a well-documented refractive index marker (Fig. 5 (b)) [36].

The ISFET “pixel” (Fig. 3), uses a source follower configuration, M_{1i} and M_{2i} , where M_{1i} is an ion sensitive transistor with its floating gate connected to a four-metal-layer stack in contact with the silicon oxide (SiO₂) layer. The sensor determines the ionic concentration above the passivation layer by measuring the change in current resulting from a change in the threshold voltage of the transistor and the gate capacitance[37]. The circuit incorporates a transmission gate for column addressing. Scanning of the array is achieved with two 4-bit decoders addressing the columns and rows via a 16-to-1 analog multiplexer located outside the array aperture. As for the SPAD array, the ISFET array incorporates the deep n-well layer of the HV process to reduce crosstalk from other sensors (Fig. 4 (b)).

The chip was fabricated using a commercially available HV CMOS 350 nm 4-metal process (H35, AMS, Premstaetten, Austria). The triple-well HV process not only enabled the use of high voltages for the SPAD’s Geiger mode, but it also allowed for the interleaved integration of separate sensor arrays, using individual circuit-isolating deep n-wells. Each sensor element is laid out in a 110 μm x 110 μm square; the SPAD,

PD, and ISFET sensors comprise active areas of 314 μm^2 , 54 μm^2 and 484 μm^2 , respectively. The total area of the final array is 1.76 x 1.76 mm². The chip has only 55 pads for power supply, control and output signals. Pads were only placed on two opposing sides of the CMOS chip so as to ease microfluidic channel integration. Separate power supply pads were used for each type of sensor and its accompanying circuits to ensure independent operation and manage the effective delivery of power.

Chips fabricated in the AMS H35 process have a polyimide top layer preventing access to the desired ISFET passivation layer. Having different sensors interleaved in the array proved to be challenging in terms of post-processing fabrication for the ISFET since the SPAD’s doped regions could be affected by reactive ion etch steps. An opening in the polyimide layer over the active area of each ISFET was therefore included in the design layout sent to the foundry. This opening comes at the cost of removing all the other passivation layers from the top metal layer (M_4), including the Si₃N₄ and SiO₂, as shown in

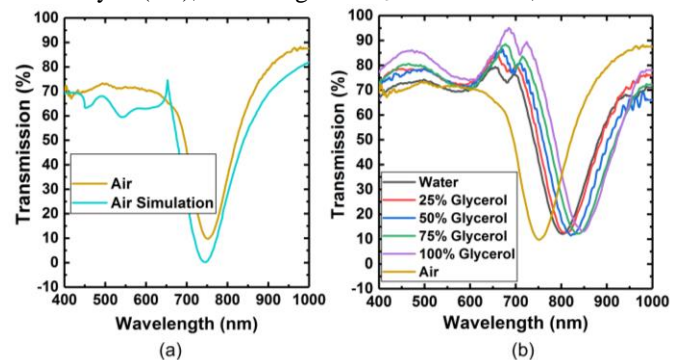


Fig. 5. (a) Simulated and measured transmission spectra of fabricated nanodiscs on a glass slide. (b) Measured resonant wavelength shift as a function of glycerol concentration of nanodiscs on a glass slide.

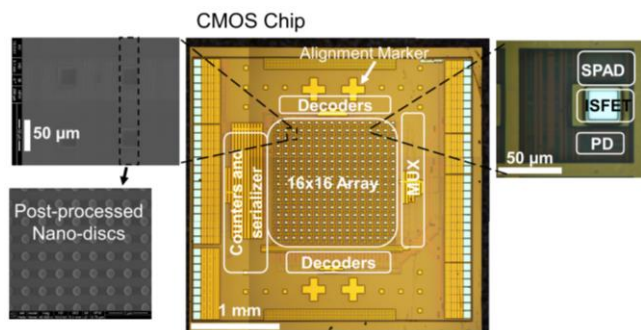


Fig. 6 Photomicrograph of the multimodal 16 x 16 element array chip, with (right) a magnified photomicrograph of a single element incorporating ISFET, PD and SPAD and (left) photomicrographs showing postprocessed elements where nanodiscs were fabricated selectively on alternate columns.

Fig. 4(b), (i). An additional SiO_2 membrane layer was exposed under M_4 by etching away the M_4 aluminium (Al) as illustrated in Fig. 4 (b), (ii) using a wet etch process of $\text{H}_2\text{O}:\text{H}_3\text{PO}_4:\text{HNO}_3:\text{CH}_3\text{COOH}$ solution in the ratio 2:16:1:1. To protect the Al bond pad contacts, photoresist was spun on and an opening was created over the ISFETs prior to the etching process. The resulting ISFET structure is shown in Fig. 4 (b), (iii), illustrating elements located in the odd columns of Fig. 2.

The fabricated CMOS chip is shown in Fig. 6, including photomicrographs detailing one of its array elements and the results of post-processing.

IV. OPTICAL, ELECTRICAL AND ELECTROCHEMICAL PERFORMANCE OF CHIP

All of the sensor types on the chip were independently evaluated. Since arrays of sensors were used, device-to-device variability known as fixed pattern noise (FPN) is expected [38]. For an imaging device FPN manifests itself as reduced picture quality. In addition to FPN, thermal noise is predominant in ISFETs and shot noise is predominant in the PDs and SPADs [39], [40]. In this work we do not want image data hence we have exploited the array to average all the signals from each sensor array to produce a single measurement with reduced noise [41]. The averaging process reduces the standard deviation of the overall measurement since the noise sources have a Gaussian distribution for large populations [42]. In addition to averaging over the different sensors used in each sensor array, we also sampled each sensor in a frame multiple times over a time interval, and averaged these too so as to produce a single measurement. Frame averaging in time intervals where events are relatively static has already been proven to improve noise in sensor data processing [43], [44]. Since the PD circuit is operated using a non-zero bias voltage, an offset is determined from the first measured frame; the same offset voltage is removed from all subsequent frames prior time-averaging [45], [46]. The method is also used for the ISFET. In an analogous method, the count rate from the first frame measured from the SPAD is used as a datum reference.

To evaluate the ISFET pH sensitivity, the chip was tested with five buffer solutions with pH values 5, 6, 7, 8 and 9. A silver/silver chloride (Ag/AgCl) reference electrode was used

biased at ~ 1.3 V with respect to the ISFET source voltage. Prior to testing the sensor, the chip was washed with DI water, dried with N_2 and then tested in the pH 9 buffer to establish a baseline. Variations in the measured voltage from 3 devices were equalized for the measurement at pH 9 in order to measure the relative change in voltage with decreasing pH in subsequent measurements. The test was repeated using the remaining buffers in order of descending pH. The data from the three ISFETs was averaged using 500 samples per pH point per device. The data showed a pH sensitivity of 33 mV/pH with a linear response between pH 5 and pH 9 as shown in Fig. 7 (a) when tested against a commercial pH probe (HI5522, HANNA instruments, Italy).

To test the dynamic range of the optical devices a monochromator was configured at a wavelength of 550 nm and attached to an optical integrating sphere to ensure uniform light distribution. An optical power meter (1936-R, Newport, USA) was fitted to one exit port to measure the light intensity. The CMOS chip was placed at another exit port. PD and SPAD sensor arrays were sampled for 100 frames each and averaged. In dark conditions, the output of the PD was $408 \text{ mV} \pm 22 \text{ mV}$. By gradually increasing the light intensity, the minimum detectable optical power density for the photodiode was measured at $50 \text{ nW}/\text{cm}^2$ using the method described by Dandin and Abshire [47]. The PD signal started to saturate when exposed to $4.9 \text{ } \mu\text{W}/\text{cm}^2$. The SPAD dynamic range was measured similarly and with the same single-wavelength light source. The SPAD array was activated and biased at 21.5 V (i.e. 3 V above its breakdown voltage). The optimum values of quenching voltage, V_q , and comparator threshold voltage, V_{trig} , were determined experimentally to be 1.20 V and 0.60 V respectively. In dark conditions, the SPAD produced a dark count rate (DCR) of $10 \text{ kcps} \pm 9.4 \text{ kcps}$. By gradually

TABLE I
SENSOR CHARACTERISATION PARAMETERS

	Parameter	Min	Typical	Max	Unit
	Chip size		3.4 x 3.6		mm^2
	Active pixel area		46		μm^2
	Array size		16 x 16		
PD	Detectable light	0.05		4.9	$\mu\text{W}/\text{cm}^2$
	Frame rate		16		fps
	Active pixel area		119		μm^2
	Array size		16 x 16		
SPAD	Detectable light	0.45		600	nW/cm^2
	Frame rate		3		fps
	Sensitivity	30.8	33	35	mV/pH
	Array size		16 x 16		
	Ref. Electrode		Ag/AgCl		
	Frame rate		42		fps
	Array size		8 x 16		
Nanodisc array	Resonant wavelength	770	780	790	nm
	Measurement Resolution- PD		2.2×10^{-4}		RIU
	Measurement Resolution- SPAD		3.8×10^{-5}		RIU

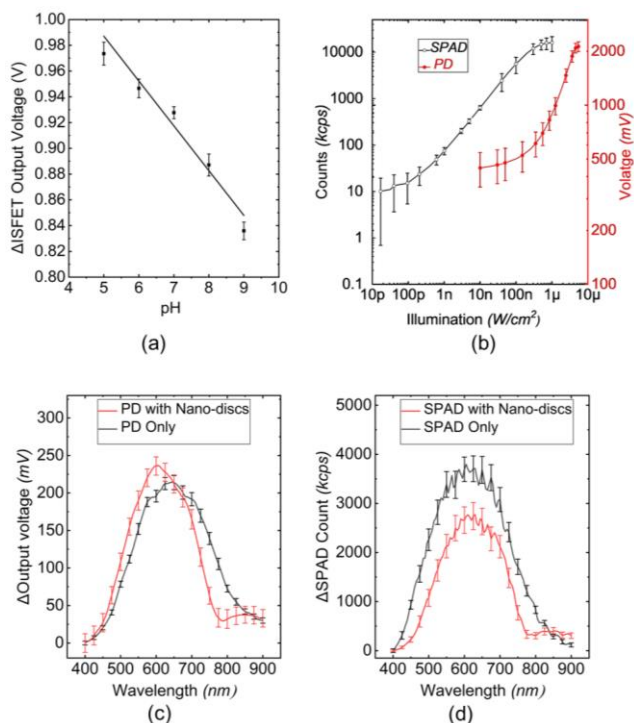


Fig. 7. Characterization and performance evaluation of the CMOS platform. (a) Measured characterization of the ISFET sensor showing an output voltage which is a linear function of pH with a sub-Nernstian slope of 33 mV/pH. (b) Measured extended optical dynamic range of the SPAD and the PD. (c) Response of PD with nanodiscs shows a dip at \sim 785 nm. (d) Count rate of SPAD with nanodiscs shows a dip at \sim 780 nm.

increasing the light intensity, the minimum detectable optical power density for the SPAD was 450 pW/cm^2 . The SPAD started to saturate with its output dominated by unwanted after-pulsing at a maximum detection rate of 15.3 Mcps corresponding to 600 nW/cm^2 .

The results show that the SPADs can detect substantially lower light levels than the PDs, making SPADs suitable for applications with low illumination intensity that require high sensitivity. In a complementary manner, the PDs are suitable for applications with high illumination intensity requiring less sensitivity. Together, they maximize the flexibility of the CMOS chip. The measured dynamic range of PD and SPAD arrays at 550 nm are reported in Fig. 7(a) and detailed in Table I.

The signals from an unpatterned PD sub-array and a PD sub-array with nanodiscs, each with 25 pixels, were measured over the optical band 400 - 900 nm. As can be seen both the devices show a peak voltage at approximately 630 nm, but only the device with nanodiscs shows an additional SPR minimum at 785 nm (Fig. 7(c)). Similarly, a pair of SPAD sub-arrays with 128 pixels, without and with added nanodiscs, show a peak at approximately 630 nm. The SPADs with nanodiscs show a minimum at 780 nm (Fig. 7 (d)).

The post-processing for the nanodiscs alters the overall apparent sensitivity of the arrays as a consequence of the well-known E-field field enhancement characteristics at resonance [48]. A small discrepancy between the PD and SPAD sensors with nanodiscs is a consequence of slight process variation. Because the nanodisc arrays require post-processing steps

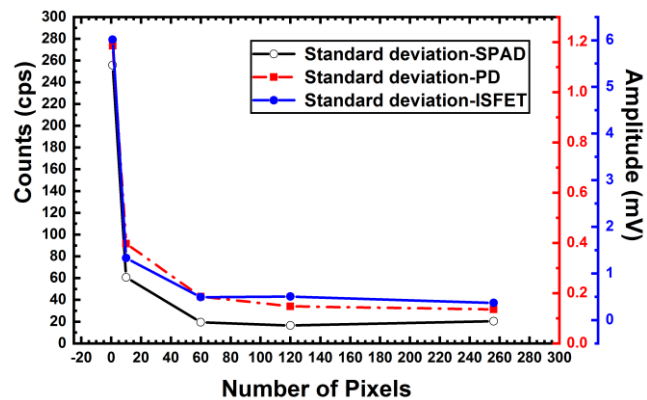


Fig. 8. Standard deviations of averaged measurements as functions of the number of sensors for the SPAD array, PD array and ISFET array

including electron beam lithography, metal deposition and lift-off, there may be some modification to PD and SPAD characteristics, the detailed study of which are outside the scope of this paper. Direct comparison of the measured transmission data shown in Fig. 5 is not possible for the chip since the silicon is not transparent. However, the PD and SPAD data clearly show spectral characteristics with the same main features.

The benefits of averaging for arrays of sensors as a function of the number of sensor pixels is illustrated in Fig. 8. It can be seen that the standard deviation that represents the signal noise, measured in volts, or in the case of the SPADs, cps, decreases as the number of pixels increases. The averaging process reduced the noise as a function of $N^{-1/2}$, where N is the number of sensors, as expected for Gaussian noise sources.

V. DIAGNOSTIC PLATFORM

A complete diagnostic platform was implemented to enable biological experiments and to demonstrate a diagnostic point of care prototype for rapid biomarker detection. The platform consists of a disposable cartridge, a reader for data acquisition and control and a portable computer to visualize the results. The cartridge comprises the CMOS chip and a ceramic pin grid array chip carrier (CPGA 120, Spectrum Semiconductor Materials Inc., USA). The chip was fabricated using a high-voltage CMOS process (H35, Austria Microsystems, Austria). A biocompatible epoxy (EPO-TEK H74, Epoxy Technology Inc., USA) was used to protect the chip wire-bonds and to fix a culture ring around the chip for aqueous measurements in a cavity created on the chip's surface, using the procedure detailed in [37]. The reader incorporates a printed circuit board (PCB) to host the post-processed chip and an ARM Mbed microcontroller (STM32 Nucleo-F334R8, STMicroelectronics, UK). The Mbed microcontroller is programmed to provide addressing signals and to acquire output readings from the arrays. A 12-bit analog-to-digital converter (ADC) incorporated in the Mbed converts the analog PD and ISFET sensor output readings to digital signals. This digital data along with the SPAD digital outputs are transferred via USB to a laptop in which they are processed and analysed via a LabVIEW application (National Instruments, Austin, TX, USA). The USB link also provides power for the chip and Mbed microcontroller. The complete diagnostic platform used in this work is shown in

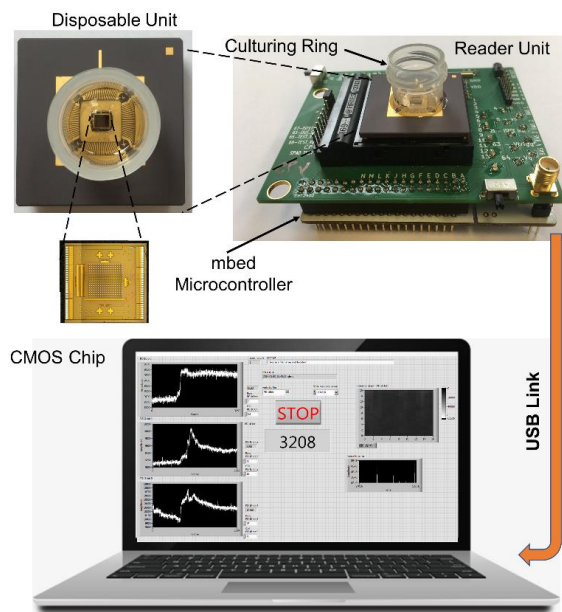


Fig. 9. A photograph of the diagnostic platform that includes the disposal unit, reader and laptop for visualization of the acquired results.

Fig. 9. Its timing diagram for one frame acquisition is illustrated in Fig. 10.

VI. BIOLOGICAL EXPERIMENTS

We performed experiments for metabolite detection to prove the chip's capabilities in its various sensing modes. Urate, cholesterol and urea-urease metabolites were used for chemiluminescence, colorimetric and H^+ measurement modes. Instead of showing reaction rates [49], [50] real time measurement signals were plotted to demonstrate the performance of each sensor. The SPR mode was demonstrated with glycerol. In addition to single mode measurements, we also showed that the platform can detect two metabolites simultaneously, using glucose and cholesterol. The implemented diagnostic platform was used and in the configured setup shown in Fig. 11 to conduct the biological experiments. The reference electrode used for a modality measurement that involves the ISFET array whereas the monochromator was used for colorimetric and SPR measurements.

A. Chemiluminescence mode

The chemiluminescence mode was demonstrated by detecting uric acid. A low level of this metabolite in human blood is an indication of Parkinson's disease[51] and elevated levels can be a risk indicator for cardiovascular, kidney disease and acute gout. In a chemiluminescent assay, luminol must be activated with an oxidant, which is usually a solution containing hydrogen peroxide (H_2O_2). In this study, a uric acid-uricase enzymatic reaction was used to produce H_2O_2 . Prior to the measurement, the chip was cleaned with acetone and isopropyl alcohol (IPA). Then a solution comprising 900 μL of 100 μM uric acid in 50 mM triethanolamine pH 8.5, 50 μL of 60 units/mL peroxidase enzyme solution, and 50 μL of 8mM luminol solution was placed onto the sensor surface. After a stable baseline was obtained, 50 μL of 1 units/mL uricase enzyme solution was added to initiate the reaction. The blue glow from the reaction was detected by the SPAD. The 100 μM , 500 μM and 1 mM concentrations of uric acid were used to cover the physiological ranges, 208 - 428 μM for males and 155 - 357 μM for females[52]. Fig. 12 (a) shows the reaction curves of the two concentrations and a control baseline.

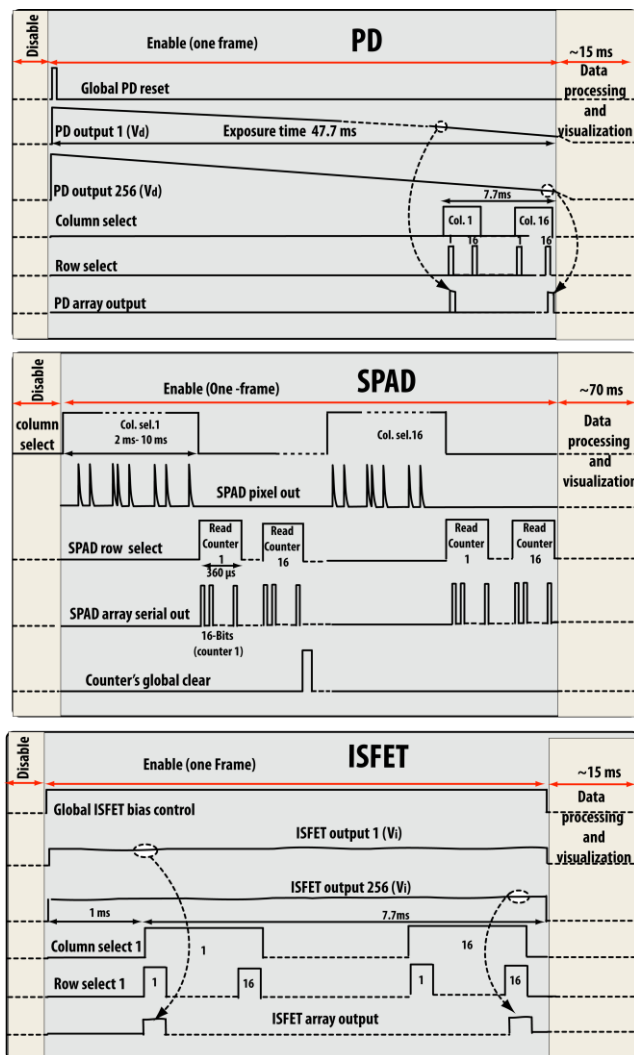


Fig. 10. System timing diagram of a single frame acquisition for PD, SPAD and ISFET array. The reported required times for data processing and visualization are average values that are dependent on the speed of the device (i.e laptop, tablet or phone) used.

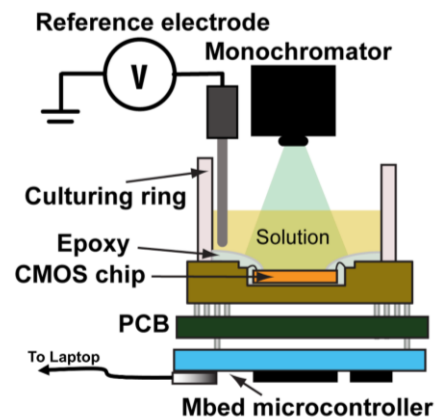


Fig. 11. Setup used to validate the use of the CMOS platform for different modalities.

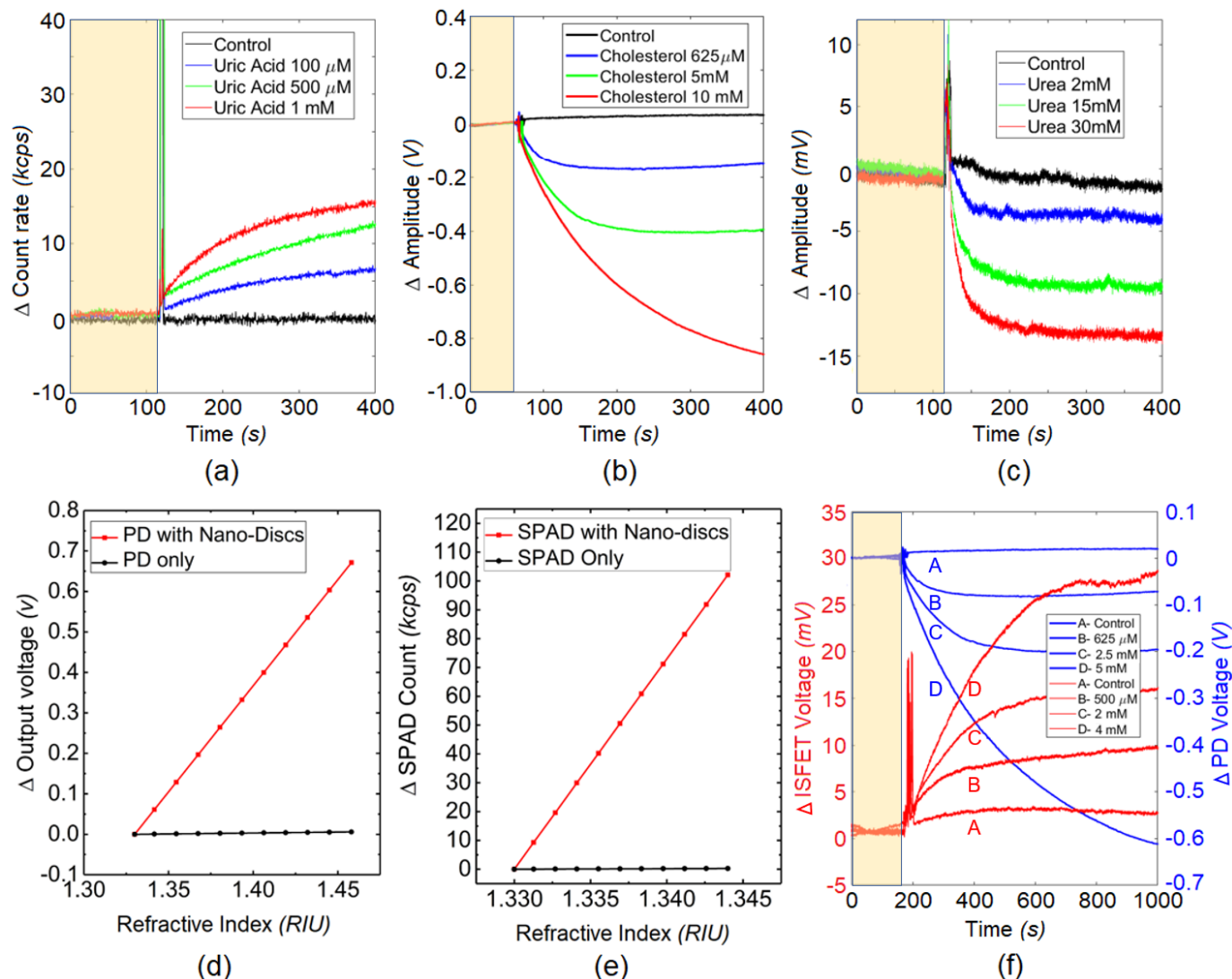


Fig. 12. Biological experiments results. (a) SPAD array response as a function of three different urate concentrations, with control experiment response. (b) PD array response for different cholesterol concentrations. (c) ISFET array response for different urea-urease concentrations. (d) PD response as a function of change in refractive index: glycerol concentrations of (0 - 100%) were measured with recorded sensitivity of 5.3 V/ RIU and resolution of 2.2×10^{-4} RIU. (e) SPAD response as a function of change in refractive index. The SPAD has a higher sensitivity of 7.3 Mcps/RIU which corresponds to a resolution of 3.8×10^{-5} RIU. (f) Real-time detection of three concentrations of human serum samples and one control sample. The signals derived from the glucose-hexokinase (red curves) and cholesterol-cholesterol oxidase (blue curves) interactions were recorded simultaneously by the ISFET and PD sensors. In (a), (b), (c) and (f), the yellow area indicates time until the serum sample was added.

B. Colorimetric mode

The colorimetric mode was demonstrated by the detection of a cholesterol metabolite in human serum; a high level is indicative of cardiovascular disease[53]. Detecting this metabolite depends on H_2O_2 which is commonly generated in many enzymatic assay reactions. When combined with peroxidase and redox colour-change indicators, the rate of the evolution of H_2O_2 can be detected by the PD array. Cholesterol-cholesterol oxidase reaction was undertaken to produce H_2O_2 .

Prior to the measurement, the chip was cleaned with acetone and IPA. Then a solution comprising 830 μ L of 20 mM triethanolamine pH 8.5, 40 μ L of 10 mM cholesterol with 10% (w/v) triton X-100, 50 μ L of 60 units/mL peroxidase enzyme solution, and 40 μ L of 7.89 mM o-Dianisidine solution was placed onto the sensor surface. After a stable baseline was obtained, 40 μ L of 10 units/mL cholesterol oxidase enzyme

solution was added to initiate the reaction. The reaction generated a brown colour that was detected by the PD illuminated with a green light from a monochromator at 500 nm.

Concentrations of 625 μ M, 5 mM and 10 mM were used to cover the physiological range, which is below 5.17 mM [54]. The reaction curves of the two concentration levels and the control baseline are shown in Fig. 12 (b).

C. Hydrogen ion measurement mode

The hydrogen ion measurement mode was demonstrated using urea-urease which is an important compound in metabolic processes; a high concentration in blood is a significant indicator of renal and heart diseases [55]. The urea-urease metabolic activity tends to increase the H^+ ion concentration of its solution as it produces ammonia, which is a basic molecule. Therefore, the urea-urease reaction was used for ISFET studies.

Prior to measurement, the chip was cleaned with acetone and IPA. The potential of the Ag/AgCl reference electrode was set to 0 V. To start the experiment, 950 μL of 30 mM urea in 50 mM triethanolamine pH 8.5 was firstly placed on the sensor surface. After a stable baseline was obtained, 50 μL of 80 units/mL urease enzyme solution was added to initiate the reaction. A decrease of the voltage signal was detected by the ISFET. Similarly to the previous metabolites, the three concentrations of urea-urease, at 2 mM, 15 mM and 30 mM, were used to bracket the physiological range, 4.98 - 6.64 mM. The results, including a control baseline, are shown in Fig. 12 (c). The long-term pH drift was measured to be 0.8 mV/hour [37] which is negligible compared to the actual measurement signal.

D. Surface plasmon resonance mode

SPR sensors on chip were used to demonstrate that the detected signal varied in response to changing the local refractive index around the metal structures. Experiments were performed using glycerol in water. The refractive index of glycerol in water as a function of the glycerol concentration is well-known [31]. Variation in refractive index is measured in refractive index units (RIU). As it can be seen in Fig. 7(c), the SPR structure introduces a minimum in the spectral response measured by the PD or SPAD at 780 nm. In this experiment a monochromator is set to emit at 780 nm, and the PD or SPAD signal is recorded as a function of the variation in the glycerol concentration, or refractive index. In this manner the SPR structure's response to varying refractive index is measured on-chip, analogous to the demonstration on glass shown in Fig. 5.

Figs. 12 (d) and (e) show the light intensity as a function of the refractive index change for the PD and SPAD with nanodiscs, respectively. In each case an offset has been introduced such that zero corresponds to the voltage or count rate in the presence of pure water. The graphs show the change in signal observed with varying refractive index. For the PD device we measured a signal change of 5.3 V/RIU and a resolution of 2.2×10^{-4} RIU. For the SPAD we observe a change in count rate of 7.3 Mcps/RIU, and we were able to resolve a change in refractive index of 3.8×10^{-5} RIU. Measurements from a PD and a SPAD without nanodiscs exhibited insignificant sensitivity to variation in the refractive index. Unlike other modalities provided by the chip, measurements from the nanodisc functionalised sensors were taken from a single sensor in the array. The experiment was repeated three times and averaged. The sample interval for the PD measurement was 0.20 s and 1 second for the SPAD.

E. Simultaneous Metabolite Detection in Human Serum

Detecting more than one metabolite simultaneously provides another demonstration of the added value of the platform. To demonstrate this, we developed an assay in which cholesterol and glucose are detected simultaneously in human serum. Two human serum samples and one control sample (without cholesterol or glucose) were detected by the ISFET and PD individually. Serum cholesterol and glucose can be detected and quantified by the two sensors simultaneously and independently. Human serum with 5 mM cholesterol and 4 mM glucose was diluted by a factor of 2 and 8 to give 2.5 mM, 625 μM cholesterol and 2 mM, 500 μM glucose.

The reaction buffer was prepared by mixing together the following enzymes and chemicals which are required for simultaneous glucose and cholesterol detection measurements: 46.9 μL of 5mM triethanolamine HCl at pH 8, 1.7 μL of 15% w/w taurocholic acid solution, 1.7 μL of 15% w/w cholic acid solution, 5 μL of 60units/mL peroxidase, 10 μL of 500 mM NaCl, 1.7 μL of 8.5 units/mL cholesterol esterase, 10 μL of 100 mM MgCl_2 solution, 10 μL of 100 mM ATP pH8.5, 4 μL of 7.89 mM o-Dianisidine, 1 μL of 0.1 units/ μL hexokinase, and 3 μL of 10 units/mL cholesterol oxidase.

The reaction buffer was added to the sensing well at time considered as $t = 0$ to obtain baselines for both the ISFET and PD. The human serum sample was added to initiate the reactions. Both the ISFET and PD generated signal changes immediately. The enzymatic reactions were measured through the change in voltage as a function of time.

As in previous measurements, the concentrations covered the physiological ranges of both metabolites [56]. Fig. 12 (f) shows the results for the high and low concentrations of both metabolites detected simultaneously.

A control baseline was established with a buffer solution for experiments conducted in this Section. The lowest detectable concentration in each experiment was chosen to be higher than 3.5 times the standard deviation of the control baseline, set as the limit of detection (LOD).

VII. CONCLUSION

The ability to rapidly detect multiple metabolites using the same instrument has a potential to reduce diagnosis time and its cost. CMOS technology allows for the integration of different types of sensors on a single chip to achieve this function, replacing large, expensive laboratory systems. For the first time we show that multi-sensor elements can be used to create a multimodal sensor on a single CMOS chip for use in biochemical assay by analysing correlated data. In addition to incorporating ISFETs to detect proton release in enzymatic assays, each element of the array format chip contains a photodiode and a SPAD. Uniquely, by integrating these two optical sensor types, it is possible to extend the dynamic range, hence utility, of the device by 1.5 decades. Each optical sub-array was further functionalized by the addition of gold nanodiscs to introduce an SPR modality. Altogether, the system enables chemiluminescence, colorimetric, SPR based and electrochemical measurements of the same analyte, all of which have been experimentally evaluated. The system's ability to quantify urea, cholesterol and urate within the human physiological range was demonstrated. Quantification of glycerol in a solution with water was also demonstrated to validate SPR sensing. With five physical sensors, each of which can be biofunctionalized independently, we have demonstrated a highly capable route towards a comprehensive point-of-care metabolomic test system for use in medical diagnostics.

REFERENCES

- [1] N. Nath and A. Chilkoti, "A colorimetric gold nanoparticle sensor to interrogate biomolecular interactions in real time on a surface," *Anal. Chem.*, vol. 74, no. 3, pp. 504–509, Feb. 2002.

- [2] S. Beck, T. O’Keeffe, J. M. Coull, and H. Köster, “Chemiluminescent detection of DNA: application for DNA sequencing and hybridization,” *Nucleic Acids Res.*, vol. 17, no. 13, pp. 5115–5124, Jul. 1989.
- [3] M. N. Valeur, B. and Berberan-Santos, “Steady-state spectrofluorometry,” in *Molecular Fluorescence*, Weinheim, Germany: Wiley-VCH Verlag GmbH & Co. KGaA, 2012, pp. 263–283.
- [4] J. Homola, “Surface plasmon resonance sensors for detection of chemical and biological species,” *Chem. Rev.*, vol. 108, no. 2, pp. 462–493, Feb. 2008.
- [5] X. Zhang, H. Ju, and J. Wang, *Electrochemical sensors, biosensors and their biomedical applications*. Elsevier/Academic Press, 2008.
- [6] P. K. Gupta, “Single-molecule DNA sequencing technologies for future genomics research,” *Trends Biotechnol.*, vol. 26, no. 11, pp. 602–611, Nov. 2008.
- [7] P. B. Lippa, L. J. Sokoll, and D. W. Chan, “Immunosensors—principles and applications to clinical chemistry,” *Clin. Chim. Acta*, vol. 314, no. 1–2, pp. 1–26, Dec. 2001.
- [8] E. Yoo and S. Lee, “Glucose biosensors: an overview of use in clinical practice,” *Sensors*, vol. 10, no. 5, pp. 4558–4576, May 2010.
- [9] R. Kaddurah-Daouk, B. S. Kristal, and R. M. Weinshilboum, “Metabolomics: A global biochemical approach to drug response and disease,” *Annu. Rev. Pharmacol. Toxicol.*, vol. 48, no. 1, pp. 653–683, Feb. 2008.
- [10] J. Wang, “Electrochemical glucose biosensors,” *Chem. Rev.*, vol. 108, no. 2, pp. 814–825, Feb. 2008.
- [11] S. R. Weinberger, T. S. Morris, and M. Pawlak, “Recent trends in protein biochip technology,” pp. 395–416, 2000.
- [12] X. Yu, N. Schneiderhan-Marra, and T. O. Joos, “Protein microarrays for personalized medicine,” *Clin. Chem.*, vol. 56, no. 3, pp. 376–387, 2010.
- [13] H. J. Lee, A. W. Wark, and R. M. Corn, “Microarray methods for protein biomarker detection,” *Analyst*, vol. 133, no. 8, p. 975, Aug. 2008.
- [14] U. Roessner and J. Bowne, “What is metabolomics all about?,” *Biotechniques*, vol. 46, no. 5, pp. 363–365, Apr. 2009.
- [15] R. F. Boyer, *Biochemistry laboratory: modern theory and techniques*, 2nd Editio. Pearson, 2012.
- [16] N. Pires, T. Dong, U. Hanke, and N. Hoivik, “Recent developments in optical detection technologies in lab-on-a-chip devices for biosensing applications,” *Sensors*, vol. 14, no. 8, pp. 15458–15479, Aug. 2014.
- [17] M. Dole, “The early history of the development of the glass electrode for pH measurements,” *J. Chem. Educ.*, vol. 57, no. 2, p. 134, Feb. 1980.
- [18] A. J. Bard, L. R. Faulkner, J. Leddy, and C. G. Zoski, *Electrochemical methods: fundamentals and applications*, vol. 2. Wiley New York, 1980.
- [19] K. Khun *et al.*, “Potentiometric glucose sensor based on the glucose oxidase immobilized iron ferrite magnetic particle/chitosan composite modified gold coated glass electrode,” *Sensors Actuators B Chem.*, vol. 173, pp. 698–703, Oct. 2012.
- [20] C. M. Lopez *et al.*, “A multimodal CMOS MEA for high-throughput intracellular action potential measurements and impedance spectroscopy in drug-screening applications,” *IEEE J. Solid-State Circuits*, vol. 53, no. 11, pp. 3076–3086, Nov. 2018.
- [21] J. S. Park *et al.*, “Multi-parametric cell profiling with a CMOS quad-modality cellular interfacing array for label-free fully automated drug screening,” *Lab Chip*, vol. 18, no. 19, pp. 3037–3050, 2018.
- [22] J. S. Park *et al.*, “1024-pixel CMOS multimodality joint cellular sensor/stimulator array for real-time holistic cellular characterization and cell-based drug screening,” *IEEE Trans. Biomed. Circuits Syst.*, vol. 12, no. 1, pp. 80–94, Feb. 2018.
- [23] X. Huang, H. Yu, X. Liu, Y. Jiang, M. Yan, and D. Wu, “A dual-mode large-arrayed CMOS ISFET sensor for accurate and high-throughput pH sensing in biomedical diagnosis,” *IEEE Trans. Biomed. Eng.*, vol. 62, no. 9, pp. 2224–2233, Sep. 2015.
- [24] T. Tokuda, K. Tanaka, M. Matsuo, K. Kagawa, M. Nunoshita, and J. Ohta, “Optical and electrochemical dual-image CMOS sensor for on-chip biomolecular sensing applications,” *Sensors Actuators A Phys.*, vol. 135, no. 2, pp. 315–322, Apr. 2007.
- [25] J. Monk, “Developments in microelectronics technology and the economics of the semiconductor industry,” *Int. J. Soc. Econ.*, vol. 7, no. 1, pp. 13–23, Jan. 1980.
- [26] P. A. Hammond, D. Ali, and D. R. S. Cumming, “A system-on-chip digital pH meter for use in a wireless diagnostic capsule,” *IEEE Trans. Biomed. Eng.*, vol. 52, no. 4, pp. 687–694, Apr. 2005.
- [27] C. Hagleitner *et al.*, “Smart single-chip gas sensor microsystem,” *Nature*, vol. 414, no. 6861, pp. 293–296, Nov. 2001.
- [28] J. M. Rothberg *et al.*, “An integrated semiconductor device enabling non-optical genome sequencing,” *Nature*, vol. 475, no. 7356, pp. 348–352, Jul. 2011.
- [29] M. Birkholz, A. Mai, C. Wenger, C. Meliani, and R. Scholz, “Technology modules from micro- and nano-electronics for the life sciences,” *Wiley Interdiscip. Rev. Nanomed. Nanobiotechnol.*, vol. 8, no. 3, pp. 355–77, 2016.
- [30] R. P. Horgan and L. C. Kenny, “‘Omic’ technologies: genomics, transcriptomics, proteomics and metabolomics,” *Obstet. Gynaecol.*, vol. 13, no. 3, pp. 189–195, Jul. 2011.
- [31] N. Psychogios *et al.*, “The human serum metabolome,” *PLoS One*, vol. 6, no. 2, p. e16957, Feb. 2011.
- [32] A. Nordström and R. Lewensohn, “Metabolomics: moving to the clinic,” *J. Neuroimmune Pharmacol.*, vol. 5, no. 1, pp. 4–17, Mar. 2010.
- [33] E. R. Fossum, “CMOS image sensors: electronic camera-on-a-chip,” *IEEE Trans. Electron Devices*, vol. 44, no. 10, pp. 1689–1698, 1997.
- [34] M. Puiu and C. Bala, “SPR and SPR imaging: recent trends in developing nanodevices for detection and real-time monitoring of biomolecular events,” *Sensors*, vol. 16, no. 6, p. 870, Jun. 2016.
- [35] M. Piliarik, H. Vaisocherová, and J. Homola, “Surface

- plasmon resonance biosensing,” A. Rasooly and K. E. Herold, Eds. Totowa, NJ: Humana Press, 2009, pp. 65–88.
- [36] L. F. Hoyt, “New table of the refractive index of pure glycerol at 20°C,” *Ind. Eng. Chem.*, vol. 26, no. 3, pp. 329–332, Mar. 1934.
- [37] B. C. Cheah *et al.*, “An integrated circuit for chip-based analysis of enzyme kinetics and metabolite quantification,” *IEEE Trans. Biomed. Circuits Syst.*, vol. 10, no. 3, pp. 721–730, Jun. 2016.
- [38] M. Bigas, E. Cabruja, J. Forest, and J. Salvi, “Review of CMOS image sensors,” *Microelectronics J.*, vol. 37, no. 5, pp. 433–451, May 2006.
- [39] M. S. Keshner, “1/f noise,” *Proc. IEEE*, vol. 70, no. 3, pp. 212–218, 1982.
- [40] R. D. Gow *et al.*, “A comprehensive tool for modeling CMOS image-sensor-noise performance,” *IEEE Trans. Electron Devices*, vol. 54, no. 6, pp. 1321–1329, Jun. 2007.
- [41] D. M. Wilson, S. Garrod, S. Hoyt, S. McKennoch, and K. S. Booksh, “Array optimization and preprocessing techniques for chemical sensing microsystems,” *Sensors Updat.*, vol. 10, no. 1, pp. 77–106, Jan. 2002.
- [42] P. Billingsley, *Probability and measure*. Wiley, 1995.
- [43] J. ~S. Lim, *Two-dimensional signal and image processing*. 1990.
- [44] J. M. Boyce, “Noise reduction of image sequences using adaptive motion compensated frame averaging,” in *[Proceedings] ICASSP-92: 1992 IEEE International Conference on Acoustics, Speech, and Signal Processing*, 1992, pp. 461–464 vol.3.
- [45] M. Schöberl, C. Senel, S. Föbel, H. Bloss, and A. Kaup, “Non-linear dark current fixed pattern noise compensation for variable frame rate moving picture cameras,” in *2009 17th European Signal Processing Conference*, 2009, pp. 268–272.
- [46] J. Richardson and J. Wallner, “Method for fixed pattern noise (FPN) correction,” 2014.
- [47] M. Dandin and P. Abshire, “High signal-to-noise ratio avalanche photodiodes with perimeter field gate and active readout,” *IEEE Electron Device Lett.*, vol. 33, no. 4, pp. 570–572, Apr. 2012.
- [48] D. M. Schaadt, B. Feng, and E. T. Yu, “Enhanced semiconductor optical absorption via surface plasmon excitation in metal nanoparticles,” *Appl. Phys. Lett.*, vol. 86, no. 6, p. 063106, Feb. 2005.
- [49] M. A. Al-Rawhani *et al.*, “A colorimetric CMOS-based platform for rapid total serum cholesterol quantification,” *IEEE Sens. J.*, vol. 17, no. 2, pp. 240–247, Jan. 2017.
- [50] C. Hu, M. A. Al-Rawhani, B. C. Cheah, S. Velugotla, and D. R. S. Cumming, “Hybrid dual mode sensor for simultaneous detection of two serum metabolites,” *IEEE Sens. J.*, vol. 18, no. 2, pp. 484–493, Jan. 2018.
- [51] S. Cipriani, X. Chen, and M. A. Schwarzschild, “Urate: a novel biomarker of Parkinson’s disease risk, diagnosis and prognosis,” *Biomark. Med.*, vol. 4, no. 5, pp. 701–712, Oct. 2010.
- [52] G. Desideri *et al.*, “Is it time to revise the normal range of serum uric acid levels?,” *Eur. Rev. Med. Pharmacol. Sci.*, vol. 18, pp. 1295–1306, May 2014.
- [53] E. S. Ford, W. H. Giles, and W. H. Dietz, “Prevalence of the metabolic syndrome among US adults,” *JAMA*, vol. 287, no. 3, p. 356, Jan. 2002.
- [54] J. Stamler, “Relationship of baseline serum cholesterol levels in 3 large cohorts of younger men to long-term coronary, cardiovascular, and all-cause mortality and to longevity,” *JAMA*, vol. 284, no. 3, p. 311, Jul. 2000.
- [55] D. Aronson, M. A. Mittleman, and A. J. Burger, “Elevated blood urea nitrogen level as a predictor of mortality in patients admitted for decompensated heart failure,” *Am. J. Med.*, vol. 116, no. 7, pp. 466–473, Apr. 2004.
- [56] H. S. Kim, “Blood glucose measurement: is serum equal to plasma?,” *Diabetes Metab. J.*, vol. 40, no. 5, p. 365, Oct. 2016.